

Surface water-ice deposits in the northern shadowed regions of Ceres

T. Platz^{1*}, A. Nathues¹, N. Schorghofer², F. Preusker³, E. Mazarico⁴, S. E. Schröder³, S. Byrne⁵, T. Kneissl⁶, N. Schmedemann⁶, J.-P. Combe⁷, M. Schäfer¹, G. S. Thangjam¹, M. Hoffmann¹, P. Gutierrez-Marques¹, M. E. Landis⁵, W. Dietrich¹, J. Ripken¹, K.-D. Matz³ and C. T. Russell⁸

Ceres, a dwarf planet located in the main asteroid belt, has a low bulk density¹, and models predict that a substantial amount of water ice is present in its mantle and outer shell^{2–4}. The Herschel telescope and the Dawn spacecraft⁵ have observed the release of water vapour from Ceres^{6,7}, and exposed water ice has been detected by Dawn on its surface at mid-latitudes⁸. Water molecules from endogenic and exogenic sources can also be cold-trapped in permanent shadows at high latitudes^{9–11}, as happens on the Moon^{12,13} and Mercury^{14,15}. Here we present the first image-based survey of Ceres's northern permanent shadows and report the discovery of bright deposits in cold traps. We identify a minimum of 634 permanently shadowed craters. Bright deposits are detected on the floors of just 10 of these craters in multi-scattered light. We spectroscopically identify one of the bright deposits as water ice. This detection strengthens the evidence that permanently shadowed areas have preserved water ice on airless planetary bodies.

Ceres has an obliquity of $4.028^\circ \pm 0.01^\circ$ (see Methods) and as a result, parts of impact crater interiors and depressions located at polar latitudes remain shaded over the course of a Ceres year (1,682 days). The Dawn spacecraft acquired images for the periods 27–37 days prior to and 27–37 days after the northern summer solstice (22 July 2015; Supplementary Fig. 1). At the solstice, shadows are at a minimum in the northern polar region. Thus, clear (panchromatic) and colour images (wavelength range 0.4–1.0 μm) from the Dawn spacecraft's Framing Camera¹⁶ at this season can be used to determine the location and extent of permanently shadowed regions and to investigate whether shadowed localized bright deposits in crater interiors — as observed in multi-scattered light and partially in illumination — are indeed water-ice deposits as predicted from simulated illumination conditions and exosphere model calculations^{10,11,17}. Cold traps are conventionally defined by H_2O loss rates of less than 1 m Gyr^{-1} , which corresponds to a temperature of less than about 110 K (ref. ¹⁸). We define permanently shadowed regions (PSRs) for those sites where the disk of the Sun never crosses the horizon (that is, terrain in the umbra but not penumbra; see details on image processing and analysis in the Methods).

Images from the Survey Orbit and High-Altitude Mapping Orbit (HAMO) imaging campaigns (Supplementary Fig. 2) were

used to create shadow maps (see Methods; Supplementary Figs 3–8). The area of PSRs based on Survey data is $1,754 \text{ km}^2$ (lower threshold value for umbra) to $2,106 \text{ km}^2$ (upper umbra threshold), or 1.35% to 1.62% of the region 65° – 90°N , respectively. The area size of PSRs based on HAMO data is 522 km^2 (lower threshold) to 569 km^2 (upper threshold) or 5.04% to 5.50% for the region poleward of 83°N (Fig. 1; see Methods for determination of upper and lower threshold values). The total estimated PSR area size (from combined HAMO and Survey datasets) is $2,129 \pm 176$ (1σ) km^2 or 0.15% of the northern hemisphere of Ceres. This is comparable to the 0.12% of permanently shadowed areas on Mercury's southern hemisphere¹⁹ and to lunar northern (0.14%) and southern (0.16%) hemispheres²⁰. The largest permanently shadowed area, about 137 km^2 (52.5% of the crater area), occurs within a crater 18 km in diameter, located at 81.75°N , 78.22°E . Permanent shadows occur almost exclusively on crater floors and pole-facing lower crater walls. All craters hosting permanent shadows were mapped on the HAMO-based average image mosaic (Fig. 2). Between 65° and 90°N , 634 craters in the size range 0.5–74 km host permanently shadowed areas; of those, 338 craters are mapped poleward of 83°N (Fig. 2). Thirty-seven craters located between 60° and 65°N may host PSRs.

Our image-based shadow analysis differs slightly from results obtained by illumination modelling¹¹, which used the stereophotogrammetrically derived HAMO shape model²¹. In ref. ¹¹, a total area of $1,800 \text{ km}^2$ is reported — approximately 15% smaller than our results obtained from Survey data using the upper umbra threshold values. Our Survey PSR map is virtually identical to the map of ref. ¹¹ except that more small-scale PSRs are recorded at polar latitudes. Since the image resolution is finer than the topography reconstructed from the same images (and insufficient representation of the terrain in shadowed regions at polar latitudes owing to poor tie-point matching), the extent of PSRs can be determined more accurately with image stacking than with illumination models, as long as enough observations near solstice at many local times are available. The HAMO PSR map (Supplementary Fig. 7) agrees with the Survey map (Supplementary Fig. 6), although more small-scale PSRs are presented in the higher-resolution HAMO dataset. At the 83°N border, PSRs match across the datasets, providing further confidence in the HAMO local time coverage

¹Max Planck Institute for Solar System Research, Justus-von-Liebig-Weg 3, 37077 Göttingen, Germany. ²University of Hawaii at Manoa, Institute for Astronomy, 2680 Woodlawn Drive, Honolulu, Hawaii 96822, USA. ³German Aerospace Center (DLR), Institute of Planetary Research, Rutherfordstrasse 2, 12489 Berlin, Germany. ⁴NASA Goddard Space Flight Center, Greenbelt, Maryland 20771, USA. ⁵The University of Arizona, Lunar and Planetary Laboratory, 1629 East University Boulevard, Tucson, Arizona 85721, USA. ⁶Freie Universität Berlin, Planetary Sciences and Remote Sensing, Malteserstrasse 74-100, 12249 Berlin, Germany. ⁷Bear Fight Institute, 22 Fiddler's Road, PO Box 667, Winthrop, Washington 98862, USA. ⁸University of California Los Angeles, Institute of Geophysics and Planetary Physics, Los Angeles, California 90024, USA. *e-mail: platz@mps.mpg.de

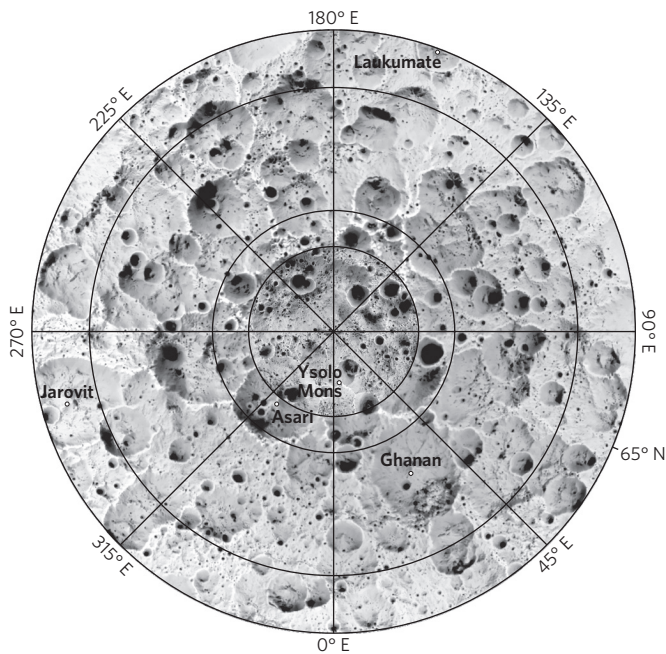


Figure 1 | Composite binary-averaged mosaic of the north polar region of Ceres. The map shows the region poleward of 65°N and is a combination of a Survey map (400 m px⁻¹) between 65° and 83°N and a HAMO map (130 m px⁻¹) northward of 83°N. Black areas are permanently shadowed regions. Latitudinal graticule is shown for 65°N, 70°N, 80°N and 83°N. A close-up of the HAMO mosaic is shown in Supplementary Fig. 7.

at this latitude (Supplementary Fig. 5; see details on assessment of illumination conditions in the Methods).

We conducted several surveys on Low-Altitude and High-Altitude Mapping Orbit (LAMO/HAMO) image data to search for potential water-ice deposits. In the first step, we created LAMO (~35 m per pixel, px) and HAMO (~140 m px⁻¹) mosaics, in which, for a given pixel location, the brightest pixels were placed on top (that is, multi-scattered light information is preserved) and candidate shadowed deposits were identified by applying various histogram stretches. In a second step, for each candidate deposit, all unprojected LAMO and HAMO images covering its location were inspected. Only 10 craters were found to host bright deposits as observed in multi-scattered light (Fig. 3, Supplementary Fig. 8). Figure 3a and b shows the most prominent bright deposit located in an unnamed crater at 86.19°N, 80.00°E. This deposit is approximately twice as bright as the surrounding crater floor material. All bright deposits in craters 1–10 (Fig. 3, Supplementary Fig. 8) are located on the crater floor off-centre towards pole-facing walls or on lower pole-facing crater wall material and so do not represent exposed target material (compare Supplementary Fig. 8q and r). Five of the ten deposits were found in craters that are not permanently shadowed at lower Survey resolution, but are probably only briefly illuminated by the Sun or are located in penumbra.

Spectroscopic information on the composition of these bright deposits is available at one location. The bright deposit in crater 2 (Fig. 3b) extends beyond the shadowed region, and its directly illuminated portion has an absolute reflectance of 0.10 to 0.16 (measured on Framing Camera imagery), which is higher than that of the bright deposits found in the Oxia crater⁷. Oxia exhibits ice-rich material spectrally detected using data from Dawn's visible/infrared mapping spectrometer, VIR⁸, which is probably forming localized haze due to water sublimation⁷. Our search for VIR data covering crater 2 yielded two observations from the Survey Orbit (1.1 km px⁻¹) in

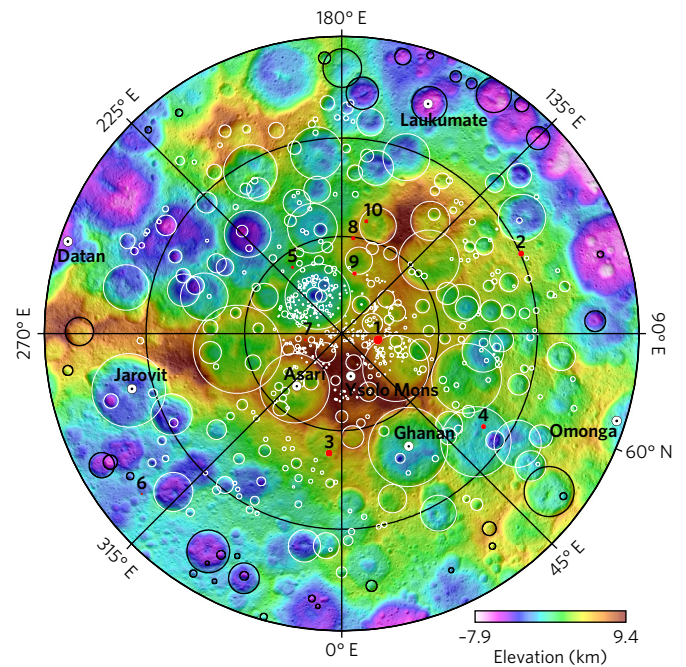


Figure 2 | Craters hosting permanent shadows and bright deposits.

This mosaic represents an average map (130 m px⁻¹) of 634 HAMO images superimposed on the HAMO DTM (~137 m px⁻¹). The map is in stereographic projection centred at the north pole and extending to 60°N. Craters hosting permanent shadows are highlighted in white. Craters containing bright deposits are shown as red filled circles (scaled to crater diameter) and are labelled 1–10. 37 craters hosting potential PSRs between 60° and 65°N are shown with black outlines.

which normalized and scaled reflectance spectra show characteristic water-ice absorption features centred at 1.28 μm, 1.65 μm and 2.0 μm (Fig. 4; see details of VIR data analysis in the Methods section). Image and spectroscopic data therefore provide *in situ* evidence for water-ice deposits adjacent to permanent shadows. Water ice on partially illuminated surfaces may be long-lasting at 70°N (crater 2), if the surface is only briefly illuminated by the Sun (Supplementary Fig. 3g). The energy flux that corresponds to an equilibrium temperature of 110 K (the threshold for water-ice stability) is at most 8 W m⁻², which in turn is produced by a Sun elevation of at most 3°. If, however, the Sun rises for only a small fraction of the Ceres year, a higher Sun elevation is still consistent with the presence of a cold trap.

The PSRs are dimly illuminated by scattered light from surrounding illuminated terrain and thermal emission from both illuminated and unilluminated terrain. We balance these sources of incoming energy with outgoing thermal emission (see Methods for details on temperature estimates for PSRs; Supplementary Table 1) to calculate an equilibrium temperature at the summer solstice. These equilibrium temperatures are an upper bound on peak summertime temperatures within the permanently shadowed regions, as the effects of energy conduction into the subsurface (which lower the peak temperature) are not accounted for. Temperatures vary with the latitude (incidence angle), the shape (bowl-shaped or flat-floored) and the depth-to-diameter ratio of the crater, but are below 57 K for all tested combinations. Ices such as H₂O, CO₂, NH₃ and SO₂ are stable for billions of years under these conditions²², although loss rates for CO₂ approach 1 m Gyr⁻¹ in our warmest cases. In contrast, obliquity variations occur on shorter timescales²³ and limit ice lifetime much more strongly than current thermal loss rates.

The north polar region is one of the most heavily cratered terrains on Ceres²⁴. The sparse distribution of bright deposits — observed only in 10 of 634 craters — in the northern hemisphere is

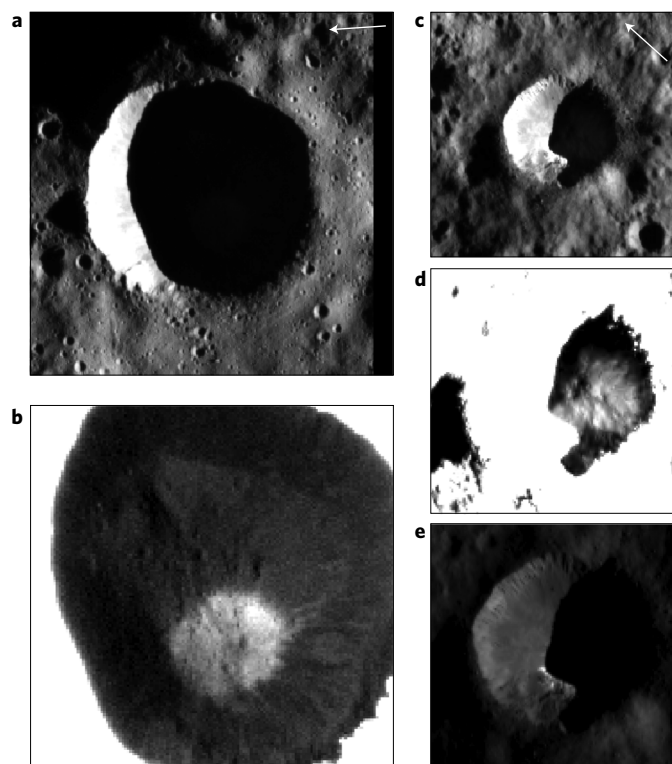


Figure 3 | Craters hosting bright deposits. **a**, Impact crater with 6.6-km diameter (crater 1; Framing Camera image 58,315) centred at 86.19° N, 80.00° E. The local time is 12:17 at the centre of the crater; local solar incidence angle is 83.1°. **b**, Close-up of the floor of the crater shown in **a**, in multi-scattered light. The crater floor exhibits a near-circular bright deposit 1.7 km in diameter. **c**, Fresh, simple, 3.8-km-diameter crater (2) located at 69.92° N, 114.04° E with bright deposit (**d**) in its shadow (Framing Camera image 57,914). **e**, A portion of the bright deposit in **d** is partially illuminated. Bright deposits are located off-centre towards pole-facing crater walls; about half the deposit is emplaced on crater wall material (see also three-dimensional anaglyph in Supplementary Fig. 8). Both images are unprojected Framing Camera images from LAMO. White arrows point to north. The locations of craters 1 and 2 are shown in Fig. 2.

surprising and plausibly the result of continuous mantling processes such as infall of ejecta material from distant impact sites, erosion as a result of direct small-scale meteoritic bombardment, space weathering or obliquity variations.

The effect of impact gardening (the churning of the crust by impacts) on the burial of ice deposits has been studied for the Moon²⁵ and Mercury²⁶. Recently, Schorghofer¹⁷ assumed the gardening rate for Ceres to be about 0.1 m Gyr⁻¹. Through asynchronous modelling of on- and near-surface temperature variations, ice loss due to diffusion, and impact gardening, ice is expected to be present in the upper 50 cm of the regolith poleward of 60° latitude, and within the upper 1 m poleward of 55° latitude¹⁷. This is consistent with previous predictions²⁷ of buried ice being present in the upper 1 m poleward of ~50° latitude. Models also predict an estimated output of retreating ice of 0.03–0.2 kg s⁻¹, of which 0.165% (PSR area of 2,129 km² in per cent, times 1.1) becomes cold-trapped in northern permanent shadows^{11,17,27}. This translates to an estimated deposition rate within permanent shadows of 1 to 5 mm Myr⁻¹. However, this is a minimum rate, as sources such as direct infall of ice-rich material and potential endogenic water could provide substantial amounts of additional water ice. For the accumulation of a 10-μm-thick ice layer in cold-traps — sufficient to raise the reflectance

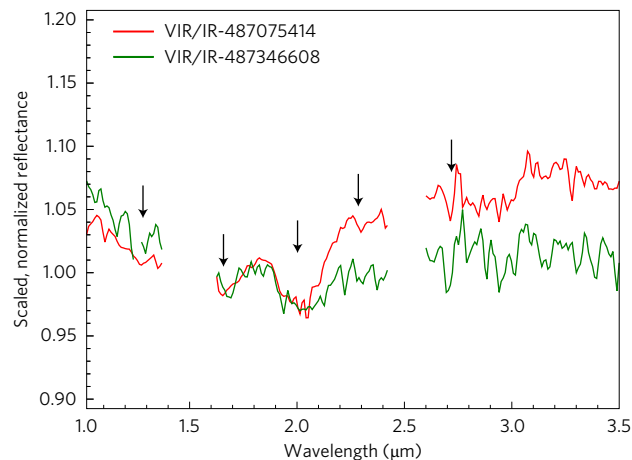


Figure 4 | Water-ice signatures within crater 2 in VIR spectra. Normalized spectra, after scaling with respect to the average spectrum of Ceres, show water-ice absorption features centred at 1.28 μm, 1.65 μm and 2.0 μm. Similar absorption features have been reported for water-ice-rich areas in the Oxo crater⁸. The absorption feature at 2.3 μm is best explained by the admixture of ammoniated phyllosilicates^{8,28}, although this feature could be due either to OH-stretching in phyllosilicates or to NH₄⁺ minerals such as NH₄Cl and NH₄CO₃ (ref. ²⁸). The absorption bands at 2.7 μm and 3.0 μm indicate the OH feature in phyllosilicates. Black arrows point to absorption features at 1.28 μm, 1.65 μm, 2.0 μm, 2.3 μm, and 2.7 μm.

to observed values — a time span of ~2 kyr to 15 kyr is required. The lower and upper time spans are plausible, as indicated by the sharp contacts between bright deposits and the surrounding crater material (Fig. 3b,d; Supplementary Fig. 8b). The lunar-derived absolute model ages²⁴ for craters 2 and 5 of 480 ka (1σ errors: +800 ka/ -400 ka) and 3.2 Ma (1σ errors: +5 Ma/ -2 Ma), respectively, imply that they are indeed old enough that they could trap sufficient ice in their shadows to be optically bright, and young enough for accumulated water-ice deposits to be minimally affected by impact gardening (see impact crater analysis in the Methods section).

Regolith mixing is a dominant process in disguising or destroying water-ice deposits. On Mercury, the presence of bright deposits, with sharp contacts, is interpreted to be the result of recent exogenic delivery of volatile inventories¹⁵. For Ceres with its high bulk water content, however, the observed sharp contacts (Fig. 3b,d, Supplementary Fig. 8b) may imply a temporary increase in the estimated water output rate or deposition rate, or both. Deposition of water-ice rich particles at polar latitudes from distant impact sites on Ceres (both endogenic and exogenic) may contribute in a substantial manner to this exogenic volatile delivery. We qualitatively assessed this scenario by simulating the impact that created the Oxo crater, located at 42.2° N, 359.6° E (Supplementary Video 2). The simulation shows that ejected particles — potentially containing a fraction of water ice in their interiors — re-impact at polar latitudes, and hence may contribute to a localized increase in water-ice deposition rate in cold traps.

The direct identification of water-ice deposits in PSRs on Ceres builds on mounting evidence from Mercury and the Moon that PSRs are able to trap and preserve water ice. For the Moon, the abundance and distribution of cold-trapped ice is little understood. On Mercury, the cold traps are filled with ice, and the planet traps about the same fraction of exospheric water as Ceres, so either the PSRs on Ceres are not able to retain as much water ice as those on Mercury or the amount of available water is much lower.

Methods

Obliquity of Ceres. The orbit of Ceres is inclined by 10.59° relative to the ecliptic plane. The spin axis, with its orientation of right ascension 291.431° ± 0.01° and

declination $66.761^\circ \pm 0.01^\circ$ (ref. ²¹), is tilted by $4.0280^\circ \pm 0.01^\circ$ with respect to the orbital axis (right ascension 293.367° , declination 62.817°).

Image processing and analysis. *Three-step image analysis strategy.* The Framing Camera on the Dawn spacecraft imaged Ceres during Rotation Characterisation 3 (RC3) from 25 April to 7 May 2015 (Supplementary Figs 1 and 2). At an orbital surface distance of $\sim 13,500$ km, Ceres's disk was covered in each image at a resolution of ~ 1.3 km px^{-1} . To assess which northern latitudes contain permanently shadowed areas, we selected in Step 1 images from the 'equatorial limb observation campaign', in which the northern hemisphere was imaged during several rotations. The last two rotations taken on 1 May 2015 with an exposure time of 280 ms (55 clear filter images) were selected and processed (see below). Persistently shadowed regions were found at latitudes northward of 56° N (Supplementary Video 1). Although these images were taken 83 days prior to passing the northern summer solstice, this Step 1 analysis provided an assessment of the latitudinal range at which shadows may persist permanently.

The northern summer solstice occurred on 22 July 2015. At this time, the Dawn spacecraft was transferring from the Survey to the High-Altitude Mapping Orbit (HAMO), and no images were taken. Therefore, images from Survey (Step 2) and HAMO (Step 3) were analysed. Step 2 analysis includes the processing of all clear filter frames (497; including off-nadir and limb observations) taken in Survey Orbit, which imaged the surface of Ceres northward of 30° N at a resolution of about 410 m px^{-1} . The Survey imaging campaign occurred from 15 to 25 June 2015, or 27–37 days prior to the northern summer solstice transit. Step 3 involved the analysis of all nadir images in clear and colour filters taken during cycle 1 of the HAMO imaging campaign from 18 to 28 August 2015, or 27–37 days past the solstice transit. All 1,716 frames covering the northern hemisphere at a resolution of ~ 140 m px^{-1} were processed.

Image processing. Framing Camera images were processed from level 1A (raw) to level 1B (radiometrically corrected) with the in-house software Calliope using parameters described in ref. ²⁹. Subsequent image processing used the Integrated Software for Imagers and Spectrometers (ISIS) developed at the US Geological Survey in Flagstaff^{30,31}. All images were map-projected onto a sphere (radius: 470 km) in Lambert azimuthal equal-area projection centred at 90° N using the stereo-photogrammetrically derived HAMO shape model²¹ with a resolution of 60 pixel per degree (~ 137 m px^{-1}) as topographic reference. Additionally, for optimal co-registration of stacked images, improved spacecraft position and instrument pointing kernels derived from Survey and HAMO stereo-photogrammetric processing were used. Because of the large footprints of Survey data (particularly for limb observations) and resulting changes in ground resolution across single images, each image was masked by a defined maximum ground resolution of 421 m px^{-1} . For HAMO images, a maximum ground resolution of 149 m px^{-1} was used.

Determining the threshold of sunlit and dark regions. Image-based analysis has been used previously to produce permanent shadow maps (see, for example, refs ^{15,32}), but the individual steps involved in determining the threshold value to distinguish a pixel as sunlit rather than dark have not been documented (except in ref. ³³). Here we report a new method for determining the threshold value for dark regions (umbra), where no direct sunlight exists.

Umbræ show a characteristic plateau in radiance profiles (cf. Supplementary Fig. 3). For each dataset, we defined the umbra threshold value within a shallow depression near the north pole at 86.1° N, 348.8° E close to the terminator. Near the pole, solar radiation is lowest. The defined threshold values (see below) are corrected for increasing solar radiation as a function of decreasing geographical latitude and longitudinal variations across a single image (that is, varying local times). The correction also accounts for the oblateness of Ceres. The instantaneous irradiation pattern captured in a single image can be found by considering the spherical law of cosines as follows. If z is the arc distance to the solar point, then

$$\frac{I(\varphi, \lambda)}{I_0} = \cos z = \cos \varphi \cos(\lambda - \Lambda_S) \cos \Phi_S + \sin \varphi \sin \Phi_S \quad (1)$$

where φ and λ are planetocentric latitude and longitude for a given image pixel, Φ_S and Λ_S are subsolar latitude and longitude at the time of image acquisition, and I_0 is the solar flux at heliocentric distance r . This rule applies to spherical bodies; however, we also consider the oblateness f :

$$f = 1 - \frac{R_{\text{pol}}}{R_{\text{eq}}} = 1 - \frac{446 \text{ km}}{482 \text{ km}} = 0.07469 \quad (2)$$

where R_{eq} is equatorial radius and R_{pol} is polar radius.

The irradiation function for oblate spheroids preserves the simple form of equation (1) (ref. ³⁴) if the planetographic latitude φ_g is used:

$$\varphi_g = \arctan\left[\frac{\tan \varphi}{(1-f)^2}\right] \quad (3)$$

resulting in:

$$\frac{I(\varphi_g, \lambda)}{I_0} = \cos \varphi_g \cos(\lambda - \Lambda_S) \cos \Phi_S + \sin \varphi_g \sin \Phi_S \quad (4)$$

This irradiation function is negative for shadowed regions (night side). The true irradiation, I_t (which is zero on the night side) can be found by calculating

$$\frac{I_t(\varphi_g, \lambda)}{I_0} = \frac{I(\varphi_g, \lambda) + |I(\varphi_g, \lambda)|}{2I_0} \quad (5)$$

For Survey data, the clear filter (F1) umbra threshold value is defined as 4.0×10^{-6} W m^{-2} sr^{-1} in image 38,829 taken on the last day of the imaging campaign (closest to summer solstice), and the profile is measured along local noon (see Supplementary Fig. 3). For the HAMO dataset, F1 and colour filters F2, F3 and F7 are used. The region northward of about 81° N was not imaged in F4, F5, F6 and F8 colour filters. The HAMO umbra threshold value for each filter is defined at the same location as for Survey. The image sequence was taken on the third day of the imaging campaign, and profiles are measured along local noon. The threshold values are: F1 = 3.5×10^{-6} W m^{-2} sr^{-1} (image 39,955), F2 = 1.4×10^{-5} W m^{-2} nm^{-1} sr^{-1} (image 39,958), F3 = 9.0×10^{-6} W m^{-2} nm^{-1} sr^{-1} (image 39,957), and F7 = 1.6×10^{-5} W m^{-2} nm^{-1} sr^{-1} (image 39,956). An image pixel is considered dark when the radiance value r is

$$r < \frac{I_t}{I_n} \quad (6)$$

where t is the threshold value for a given image dataset (see above) and x is the correction factor, with $x = 1.5$ giving the lower umbra bound and $x = 2$ the upper umbra bound, to account for variations in surface albedo and local slope (for example, more light is reflected from steep crater walls into shadowed areas relative to flat terrain). The irradiation value I_n is the value of I_t taken at the reference site at 86.1° N, 348.8° E from the reference images (see above) and is kept constant for each dataset analysis.

Each image was map-projected using a Lambert azimuthal equal-area projection centred at the north pole and binarized by applying the above threshold value and the upper- and lower-bound correction factor. Values exceeding the upper and lower umbra threshold values at a given pixel location are set to 1 (white); all remaining pixels are set to 0 (black). For each dataset, two binary mosaics (for lower and upper umbra threshold values) were produced such that the brightest pixel is placed on top (that is, white if present). The resulting binary Survey and HAMO mosaics highlight those areas in black, which are in umbra in every image during the imaging campaigns; areas in white are partially (penumbra) or fully illuminated (Supplementary Figs 6 and 7).

Figure 1 displays the average binary mosaics from 83° – 90° N (HAMO) and 65° – 83° N (Survey). Similar binary average maps were created for Mercurian¹⁵ and lunar^{32,33} polar shadowed regions and represent illumination maps over a solar day and year, respectively. However, the Cerean maps (Fig. 1) are compiled from images taken over 30 solar days at varying local times and subsolar latitudes. Therefore, these maps only show permanently shadowed regions (in black) and partially or fully lit regions (in white); grey-appearing regions do not represent the percentage of illuminated regions.

Assessment of illumination conditions. All Framing Camera image sequences during Survey, HAMO and LAMO were initiated when the Dawn spacecraft flew over the north pole of Ceres at local dawn (that is, the terminator is visible in the first images) and continued until it just passed the south pole at local dusk. As a result, image overlap at various local times is highest near the poles and lowest at the equator (that is, equatorial regions are never imaged at dusk or dawn, owing to the low angle between the Sun and the orbital plane of the spacecraft; Supplementary Fig. 2). To assess whether the locations of potential permanent shadows are imaged during local daylight between sunrise and sunset, the minimum latitude is determined for each dataset for which the density of local time coverage is sufficient. At first, the local time of each image was calculated in 5° longitude increments while keeping the latitude in each iteration constant. Based on this initial survey, local times were extracted from the images in 1° longitude and latitude increments within a narrow latitudinal range.

For Survey data, the local time coverage is considered sufficient northward of 65° N (Supplementary Fig. 4), whereas the local time coverage for HAMO data is only considered satisfactory northward of 83° N (Supplementary Fig. 5). There are instances at 65° N, where a time gap of up to 2 h in Survey coverage occurs. However, these time gaps occur close to (before and after) local sunset at 18:34 (Supplementary Fig. 4), where incident flux is minimal owing to the Sun's position near the horizon, and shadows are already much longer than their permanent extent. Two-hour local time gaps occur frequently in the HAMO dataset (Supplementary Fig. 5). However, the time spacing across the local day at 83° N is consistent between sunrise (03:41) and sunset (20:19).

Framing Camera limitations. The detection of deposits in shadowed regions is limited by a number of factors: (1) the signal-to-noise ratio of the acquired image, (2) the timing of image acquisition (for example local noon versus local sunset), (3) the amount of secondary illumination by surrounding terrain (for example from variations in material albedo and terrain slope), (4) stray light effects for colour filters and (5) compression artefacts. The compression algorithm used on the Framing Camera is such that very low signals, such as those from the shaded regions, are modified by the compression algorithm if the compression gets lossy. The compression ratio has been varied throughout LAMO imaging, but was mostly lossless or nearly lossless. To verify each positive detection of a bright deposit, the deposit has been inspected on at least seven images (typically more than 10 images) at various local times. Therefore, our search for bright shadowed deposits is considered robust.

VIR data analysis. Spectra of a directly illuminated site, adjacent to the bright deposit seen in multi-scattered light in crater 2 located at 69.92°N, 114.04°E, were studied using data from the VIR. Two VIR cubes (487075414 and 487346608) from Survey Orbit with a resolution of 1.1 km/px⁻¹ cover this location (each data cube is a stacked set of two-dimensional images). VIR calibrated and projected reflectance data (level 1C) provided to the Dawn team are not thermally corrected, and therefore our analysis is limited to 3.5 μm. Scaled spectra in Fig. 4 are calculated by dividing each VIR spectrum by its own average reflectance between 1 and 3.5 μm. The ratios are then calculated between local scaled spectra near the PSR and the scaled reflectance of the global average spectrum of Ceres²⁸, which does not exhibit any absorption bands at these wavelengths.

The shape of scaled and ratioed spectra is mostly independent of the geometry of illumination and observation, and also independent of the absolute calibration of the instrument, which is key for the detection of absorption features that represent only a few per cent of the signal amplitude and that cover a very limited area of a few square kilometres. Even if the spatial resolution of the VIR footprint is smaller than the H₂O-rich materials, it is likely that more than one VIR pixel partially covers the area, and therefore a detection is considered valid when the spectral features of H₂O are present in several contiguous pixels, indicating a spatially coherent area of similar composition. The spectrum presented in Fig. 4 is an average of four pixels. Owing to the low VIR resolution, spectra are likely to represent mixtures of bright material and dark surface material (see Fig. 4). However, absorption features centred at 1.28 μm, 1.65 μm and 2.0 μm unambiguously represent water-ice deposits.

Temperature estimates for PSRs. Thermal conditions within near-polar permanently shadowed craters vary slowly over the course of a Ceres year, and diurnal variations near the pole are minimal. A full thermal model would balance incoming and outgoing radiation with thermal conduction to the subsurface to estimate surface temperature. As thermal inertia increases, the peak temperatures experienced become lower. Thus, a useful end-member is to consider a thermal inertia of effectively zero, in order to place an upper limit on the peak temperatures. In this special case, there is no heat conduction between the surface and subsurface, and incoming and outgoing radiation are balanced at an equilibrium temperature.

The difficulty in finding this equilibrium temperature lies in calculating the incident flux, which comes mainly from scattered sunlight from surrounding illuminated terrain, and from thermal emission from both illuminated and unilluminated terrain. This energy flux warms each surface element, which in turn emits infrared radiation and reflects visible radiation that warms all the surrounding elements. One must solve for all the terrain temperatures simultaneously to account for all orders of scattered visible and emitted infrared radiation. The method for accomplishing this is known as the radiosity method and has been used previously to calculate temperatures in permanently shadowed craters on Mercury³⁵ and icy polar pits on Mars³⁶.

As examples, we tested two crater shapes (parabolic bowl-shaped, and flat-floored with 30° walls), each with two different depth-to-diameter ratios (0.1 and 0.2). Incidence angles tested were 86° (experienced at the north pole at summer solstice) as well as 69° and 79° (the minimum allowed for craters with depth-to-diameter ratios of 0.2 and 0.1 to have any permanent shadow). Direct illumination and shadowing were calculated and the radiosity method used to find incident visible light on each surface element within the crater. An initial estimate of equilibrium temperature (and outgoing infrared flux) was made from this. These outgoing infrared fluxes were used again with the radiosity method to calculate incident infrared flux on each surface element, and the surface temperatures were updated. Several iterations were required to converge on the correct answer. For the crater interiors, we used a typical Ceres albedo of 0.09 and emissivity of 0.9.

In Supplementary Table 1 we report on temperatures at the crater centre. Near-polar craters (incidence angles of 86°) experience central peak temperatures of 28–35 K, depending on their shape. At lower latitudes, the angle of incidence decreases, which results in more of a crater's wall being illuminated and greater scattered light on the centre of the crater floor. At the minimum incidence angle permitted by the freshest crater (depth-to-diameter ratio of 0.2), temperatures at

the crater centre can be as high as 57 K. At 57 K, the sublimation rates of many ices are low, roughly 0 and 0.1 m Gyr⁻¹ for H₂O and CO₂ respectively.

Several considerations mean that these peak temperatures are upper limits for the actual peak temperatures in permanently shadowed craters, since thermal inertia is never zero and conduction to the subsurface always reduces peak temperatures. As shown here, only a few of the permanent shadows contain bright deposits at their centre. These higher albedos will further reduce the real peak temperatures from the values reported here. Here, we consider the minimum possible incidence angles that preserve permanent shadow; however, at non-polar latitudes, for much of the day the incidence angle will be higher. Likewise, at seasons other than summer solstice, the incidence angles will be higher and temperatures lower. Ice stability depends on the full annual temperature profile; the sublimation rates quoted above assume peak temperature all the time and so offer a strong upper limit to the real rate of ice loss.

Impact crater analysis. For Ceres, there are currently two chronology models available to estimate absolute model ages based on crater size–frequency distributions: the lunar-derived model (LDM) and the asteroid-derived model (ADM)³⁴. The models predict that a crater ≥1.5 km in diameter (such as crater 5) would statistically be formed on the surface of Ceres every 22 kyr (LDM; ADM: 7 kyr), whereas an impact event creating a crater ≥3.8 km in diameter (such as crater 2) occurs every 256 kyr (LDM; ADM: 78 kyr). However, this would only represent the formation age of the craters if we could be certain that these two craters were the youngest on Ceres in their size range. A more robust assessment of the maximum absolute model age of crater formation can be made using the information that no superimposed craters were detected on the craters or on their ejecta blankets at the best available image resolution (35 m px⁻¹). By setting the minimum threshold pixel value to 5 to identify an impact crater (that is, we assume there exists no superimposed crater >175 m in diameter) — a reasonable value considering very good image quality and illumination conditions — the LDM model ages³⁷ for craters 2 and 5 are 480 ka (1σ errors: +800 ka/−400 ka) and 3.2 Ma (1σ errors: +5 Ma/−2 Ma), respectively. The ADM model ages are comparable (crater 2: 550 ka, +900 ka/−400 ka; crater 5: 3.7 Ma, +6 Ma/−3 Ma). Here, we used a method based on Poisson timing analysis and Bayesian inference — the exact evaluation of the crater chronology model — to derive a meaningful order-of-magnitude model³⁸.

Data availability. The data that support the plots within this paper and other findings of this study are available from the corresponding author upon reasonable request.

Received 27 June 2016; accepted 9 November 2016;
published 15 December 2016

References

- Park, R. S. *et al.* Interior structure of dwarf planet Ceres from measured gravity and shape. *Nature* **537**, 515–517 (2016).
- Thomas, P. C. *et al.* Differentiation of the asteroid Ceres as revealed by its shape. *Nature* **437**, 224–226 (2005).
- Zolotov, M. Y. On the composition and differentiation of Ceres. *Icarus* **204**, 183–193 (2009).
- Castillo-Rogez, J. & McCord, T. B. Ceres' evolution and present state constrained by shape data. *Icarus* **205**, 443–459 (2010).
- Russell, C. T. & Raymond, C. A. The Dawn mission to Vesta and Ceres. *Space Sci. Rev.* **163**, 3–23 (2011).
- Küppers, M. *et al.* Localized sources of water vapour on the dwarf planet (1) Ceres. *Nature* **505**, 525–527 (2014).
- Nathues, A. *et al.* Sublimation in bright spots on (1) Ceres. *Nature* **528**, 237–240 (2015).
- Combe, J.-Ph. *et al.* Detection of local H₂O exposed at the surface of Ceres. *Science* **353**, 3010 (2016).
- Arnold, J. R. Ice in the lunar polar regions. *J. Geophys. Res.* **84**, 5659–5668 (1979).
- Hayne, P. O. & Aharonson, O. Thermal stability of ice on Ceres with rough topography. *J. Geophys. Res.* **120**, 1567–1584 (2015).
- Schorghofer, N. *et al.* The permanently shadowed regions of dwarf planet Ceres. *Geophys. Res. Lett.* **43**, 6783–6789 (2016).
- Feldman, W. C. *et al.* Fluxes of fast and epithermal neutrons from Lunar Prospector: Evidence for water ice at the lunar poles. *Science* **281**, 1496–1500 (1998).
- Colaprete, A. *et al.* Detection of water in the LCROSS ejecta plume. *Science* **330**, 463–468 (2010).
- Paige, D. A. *et al.* Thermal stability of volatiles in the north polar region of Mercury. *Science* **339**, 300–303 (2013).
- Chabot, N. L. *et al.* Images of surface volatiles in Mercury's polar craters acquired by the MESSENGER spacecraft. *Geology* **42**, 1051–1054 (2014).
- Sierks, H. *et al.* The Dawn Framing Camera. *Space Sci. Rev.* **163**, 263–327 (2011).

17. Schorghofer, N. Predictions of depth-to-ice on asteroids based on an asynchronous model of temperature, impact stirring, and ice loss. *Icarus* **276**, 88–95 (2016).
18. Watson, K. *et al.* The behavior of volatiles on the lunar surface. *J. Geophys. Res.* **66**, 3033–3045 (1961).
19. Chabot, N. L. *et al.* Areas of permanent shadow in Mercury's south polar region ascertained by MESSENGER orbital imaging. *Geophys. Res. Lett.* **39**, L09204 (2012).
20. Mazarico, E. *et al.* Illumination conditions of the lunar polar regions using LOLA topography. *Icarus* **211**, 1066–1081 (2011).
21. Preusker, F. *et al.* Dawn at Ceres – shape model and rotational state. *47th Lunar and Planetary Science Conf.* abstract 1954 (2016).
22. Zhang, J. A. & Paige, D. A. Cold-trapped organic compounds at the poles of the Moon and Mercury: Implications for origins. *Geophys. Res. Lett.* **36**, L16203 (2009).
23. Skoglov, E., Magnusson, P. & Dahlgren, M. Evolution of the obliquity of ten asteroids. *Planet. Space Sci.* **44**, 1177–1183 (1996).
24. Hiesinger, H. *et al.* Cratering on Ceres: Implications for its crust and evolution. *Science* **353**, 4759 (2016).
25. Crider, D. H. & Vondrak, R. R. Space weathering effects on lunar cold trap deposits. *J. Geophys. Res.* **108**, 5079 (2003).
26. Crider, D. & Killen, R. M. Burial rate of Mercury's polar volatile deposits. *Geophys. Res. Lett.* **32**, L12201 (2005).
27. Fanale, F. P. & Salvail, J. R. The water regime of asteroid (1) Ceres. *Icarus* **82**, 97–110 (1989).
28. De Sanctis, M. C. *et al.* Ammoniated phyllosilicates with a likely outer Solar System origin on (1) Ceres. *Nature* **528**, 241–244 (2015).
29. Schröder, S. E. *et al.* In-flight calibration of the Dawn Framing Camera. *Icarus* **226**, 1304–1317 (2013).
30. Anderson, J. A. *et al.* Modernization of the Integrated Software for Imagers and Spectrometers. *35th Lunar and Planetary Science Conf.* abstract 2039 (2004).
31. Keszthelyi, L. *et al.* Support and future vision for the Integrated Software for Imagers and Spectrometers (ISIS). *44th Lunar and Planetary Science Conf.* abstract 2546 (2013).
32. Bussey, D. B. *et al.* Illumination conditions at the lunar south pole. *Geophys. Res. Lett.* **26**, 1187–1190 (1999).
33. Speyerer, E. J. & Robinson, M. S. Persistently illuminated regions at the lunar poles: Ideal sites for future exploration. *Icarus* **222**, 122–136 (2013).
34. van Hemelrijck, E. The oblateness effect on the solar radiation incident at the top of the atmosphere of the outer planets. *Icarus* **51**, 39–50 (1982).
35. Vasavada, A. R. *et al.* Near-surface temperatures on Mercury and the Moon and the stability of polar ice deposits. *Icarus* **141**, 179–183 (1999).
36. Byrne, S. & Ingersoll, A. P. A sublimation model for Martian south polar ice features. *Science* **299**, 1051–1053 (2003).
37. Michael, G. G. & Neukum, G. Planetary surface dating from crater size–frequency distribution measurements: Partial resurfacing events and statistical age uncertainty. *Earth Planet. Sci. Lett.* **294**, 223–229 (2010).
38. Michael, G. G. *et al.* Planetary surface dating from crater size–frequency distributions: Poisson timing analysis. *Icarus* **277**, 279–285 (2016).

Acknowledgements

We acknowledge the outstanding work of the Dawn design, engineering and operations team. We thank NASA, the Max Planck Society, and the German and Italian Space Agencies for support for this investigation.

Author contributions

T.P. designed the concept of this study, developed the threshold methodology, performed the image processing and prepared the manuscript. A.N., N.Scho., F.P., E.M., S.E.S., M.S., M.H., P.G.-M., W.D., J.R., K.-D.M. and C.T.R. contributed to the development of data analysis and interpretation. S.B. and M.E.L. performed the temperature calculations. Crater analysis and impact simulation were performed by T.K. and N.Schm., respectively. J.-P.C. and G.S.T. analysed the VIR data. All authors discussed and contributed to the preparation of this manuscript.

Additional information

Supplementary information is available for this paper.

Reprints and permissions information is available at www.nature.com/reprints.

Correspondence and requests for materials should be addressed to T.P.

How to cite this article: Platz, T. *et al.* Surface water-ice deposits in the northern shadowed regions of Ceres. *Nat. Astron.* **1**, 0007 (2016).

Competing interests

The authors declare no competing financial interests.